Int. J. Heat Mass Transfer. Vol. 35, No. 11, pp. 2865–2877, 1992
Printed in Great Britain

0017–9310/92 $5.00+0.00

A variable property analysis of alloy solidification using the anisotropic porous medium approach

S. K. SINHA and T. SUNDARARAJAN†
Department of Mechanical Engineering, Indian Institute of Technology, Kanpur-208016, India

and

V. K. GARG
Department of Mechanical Engineering, University of Pittsburgh, Pittsburgh, PA 15261, U.S.A.

(*Received* 10 *December* 1990 *and in final form* 3 *December* 1991)

Abstract—A theoretical model for heat transfer and fluid flow during alloy solidification is presented. A detailed accounting has been made for the property variations in the dendritic phase-change region. A generalized porous medium approach has been adopted, with the variation of permeability being anisotropic. The effects of anisotropy are observed to be significant if the extent of the mushy zone is large or if the Rayleigh number is high.

INTRODUCTION

SOLIDIFICATION of an alloy metal poses many formidable challenges for theoretical analysis. Unlike in pure metal systems, the phase-change occurs over a range of temperatures encompassing a finite volume. The zone where solidification takes place (known as the mushy region) comprises both the solid and the liquid phases and is characterized by the growth of finger-like (dendritic) structures [1–3]. The buoyancy-driven flow of fluid in the mushy and fully-liquid regions significantly influences the rate of solidification as well as the shape of phase fronts, during the phase-change process. The presence of the alloying component often leads to mass transfer which greatly alters the microstructure and the mechanical properties of the solidified metal. In addition, the thermodynamic and transport properties vary continuously over the whole domain of the mushy zone which needs to be taken into account in any accurate theoretical modelling.

Various approaches have been adopted to model the flow in the mushy region. The most widely-used among them are the pseudo-viscosity method [1], the velocity 'switch-off' technique [2] and the porous medium approach [3]. Of the above, the porous medium model presents the most realistic view of the resistance offered by the dendrites to the flow in the mushy zone. The porosity of the equivalent porous medium is taken equal to the volume fraction of the liquid. Evidently, the porosity is non-uniform in the mushy zone, varying from a value of unity in pure liquid to zero in the solid.

Although the variable property porous medium approach has been adopted by many recent studies of alloy solidification, the important aspect of anisotropic variation in permeability in the mushy zone has largely been ignored [4, 5]. For alloy metals, the fact that the mushy zone consists of a mixture of saturated solid and liquid phases in varying proportions, leads to a continuous variation in every thermodynamic or transport property. In addition, the strongly directional nature of the dendrites results in anisotropic permeability of the porous medium in directions parallel and normal to the dendrites [6].

In the present study, the thermal and flow aspects of two-dimensional solidification are investigated. All the important variations of properties have been taken into account, including the anisotropic nature of the mushy zone permeability. A fixed-grid methodology based on the finite element method has been implemented, which is suitable for analysing alloy solidification in any arbitrary two-dimensional geometry.

MATHEMATICAL FORMULATION

The two-dimensional solidification of an alloy material inside a rectangular enclosure with two adiabatic and two isothermal walls is considered.

† Author to whom all correspondence should be addressed.

NOMENCLATURE

A parameter as defined by equation (25)
A^e elemental area
As aspect ratio of the cavity
c specific heat
C_{11}, C_{12}, etc. elemental sub-matrix coefficients as defined by equation (32)
d_1, d_2 primary and secondary dendrite spacings
e index for element number
E total number of elements
f_1, f_2, f_3, f_4 elemental sub-matrix coefficients as defined by equation (32)
g acceleration due to gravity
h specific enthalpy; heat transfer coefficient
h_f latent heat of phase-change at solidus temperature
$\hat{j}$ unit vector along y-axis
k thermal conductivity
$\underline{\underline{K}}$ permeability tensor
K_1, K_2 tensorial components of $\underline{\underline{K}}$ in principal directions
$K_{xx}, K_{xy}, K_{yx}, K_{yy}$ tensorial components of $\underline{\underline{K}}$ in global Cartesian coordinate system
L width of the cavity
m, m_1, m_2 morphology parameters
M non-dimensional morphology parameter; linear shape function
N quadratic shape function
Nu_0 local Nusselt number on hot wall, hL/k_0
Pr Prandtl number
p, P dynamic pressure (dimensional and non-dimensional)
$\underline{\underline{R}}$ non-dimensional porous medium resistivity tensor as defined by equation (9)
$R_{xx}, R_{xy}, R_{yx}, R_{yy}$ tensorial components of $\underline{\underline{R}}$ in global Cartesian coordinate system
Ra Rayleigh number
Ste Stefan number
t time
T temperature
$\mathbf{V}$ superficial (area-averaged) velocity vector
u, v, U, V components of superficial velocity (dimensional and non-dimensional)
x, y, X, Y Cartesian coordinates (dimensional and non-dimensional).

Greek symbols
α thermal diffusivity
β coefficient of thermal expansion of liquid
γ angle made by the local gradient of temperature with x-axis
ε porosity (volume fraction of liquid)
θ non-dimensional temperature
λ latent heat of phase-change
μ viscosity
ν kinematic viscosity
ρ density
$\sigma_1, \sigma_2, \sigma_3, \sigma_4$ non-dimensional variables as defined by equation (25)
τ non-dimensional time
$\Delta\tau$ non-dimensional time-step
Ω area of the calculation domain.

Subscripts
c cold wall
h hot wall
i, j nodal indices
init initial condition
l liquid or liquidus
0, ref reference values
s solid or solidus.

Superscripts
0 value corresponding to previous time-step
$\tilde{}$ value corresponding to previous iteration
* non-dimensional normalized value.

Although mass transfer of the alloying component has important bearing upon the mechanical properties of the solidified material and also it partially affects flow and heat transfer processes, it has been ignored in the present study for the sake of simplicity. The flow field is represented in terms of the superficial velocity vector $\mathbf{V}$ (area-averaged vectorial velocity). By definition, the superficial velocity vector becomes zero in the solid region and equal to the actual velocity vector in the fully-liquid region. In the mushy zone, it depends on the local porosity and needs to be evaluated through the flow equations appropriate for a porous medium.

For a densely-packed medium with small pore-spacing, Darcy proposed that the pressure drop through the medium is directly proportional to the flow rate and fluid density, and inversely proportional to the permeability of the medium. The permeability, in turn, was defined as an intrinsic property of the porous medium which characterizes the flow resistance offered by the medium. Later modifications to Darcy's law have included the contributions of viscous and inertial stresses to the pressure gradient in the flow field [7, 8]. These are applicable for large pore-spacing (or high porosity), high flow rates and when boundary layers exist adjacent to the confining impermeable walls of the porous medium.

In the present study, the generalized Darcy's equa-

tion has been considered which bears a close resemblance to the Navier–Stokes equations, except for the term representing the resistance of the solid matrix. Such a description is essential for the alloy solidification problem since the variation of porosity across the mushy zone spans the entire possible range of zero to unity. Moreover, for the range of parameters studied herein, the inertial effects are significant and flow regions displaying boundary layer nature exist close to the walls of the enclosure [9]. Assuming the Boussinesq approximation for liquid density variation to be valid, the governing equations for flow through the anisotropic mushy zone can be represented as:

Continuity

$$\frac{\partial}{\partial t}(\rho/\rho_l)+\nabla\cdot\mathbf{V}=0 \tag{1}$$

Momentum

$$\frac{\rho}{\rho_l}\frac{\partial}{\partial t}\left(\frac{\rho_l}{\rho}\mathbf{V}\right)+\mathbf{V}\cdot\nabla\left(\frac{\rho_l}{\rho}\mathbf{V}\right)$$

$$=-\frac{1}{\rho_l}\nabla p+\nu_l\nabla\cdot\left[\frac{\rho}{\rho_l}\nabla\left(\frac{\rho_l}{\rho}\mathbf{V}\right)\right]$$

$$-g\beta(T-T_{\mathrm{ref}})-\nu_l[\underline{\underline{K}}]^{-1}\cdot\mathbf{V} \tag{2}$$

Energy

$$\frac{\partial}{\partial t}(\rho h)+\rho_l\mathbf{V}\cdot\nabla h_l=\nabla\cdot k\nabla T+h_l\frac{\partial\rho}{\partial t}. \tag{3}$$

Except for the anisotropic permeability term, these equations are similar to those derived by Bennon and Incropera [10] for alloy solidification with a stationary solid matrix in the mushy zone. In the momentum equation given above, the buoyancy contribution arising from concentration gradients of the alloying component has not been considered. This assumption can be justified if the concentration of the alloying component is very small. Some of the earlier investigators [11] have used the porous medium enthalpy h in place of liquid enthalpy h_l in the convective term of the energy equation (3). The inconsistency resulting from such usage is reported elsewhere [9].

In order to incorporate the realistic nature of flow resistance offered by the dendritic structures in the mushy zone, it is necessary to consider the permeability to be dependent on direction. For instance, Poirier [6] has shown that the permeability values are vastly different from each other (sometimes differing by orders of magnitude) in directions parallel and normal to the dendrites. Considering the dendrites as a bank of cylindrical objects and using the appropriate Blake–Kozeny pressure drop correlations, he has derived the following expressions

$$K_1=\frac{m_1\varepsilon^3}{(1-\varepsilon)^2} \tag{4a}$$

and

$$K_2=\frac{m_2\varepsilon^3}{(1-\varepsilon)^{0.75}} \tag{4b}$$

where K_1 and K_2 are respectively the permeabilities in the directions parallel and normal to the dendrites, ε is the medium porosity and m_1, m_2 are parameters which depend on the morphology of the dendrites. The parameters m_1 and m_2 can be correlated to the primary and secondary dendrite spacings d_1 and d_2 [6] through the relations

$$m_1=c_1(\varepsilon)d_1^{\mathrm{p}}d_2^{\mathrm{q}} \tag{5a}$$

and

$$m_2=c_2(\varepsilon)d_1^{\mathrm{r}}d_2^{\mathrm{s}}. \tag{5b}$$

In the region where flow is significant ($\varepsilon>0.3$), the functions $c_1(\varepsilon)$ and $c_2(\varepsilon)$ are nearly constants and therefore without much loss in accuracy constant values may be used for them. The values of the dendrite spacings d_1, d_2 and the exponents p, q, r, s depend on the nature of the alloy system. For a typical system such as Pb–Sn alloy, it turns out that $m_1\simeq m_2$ if d_1/d_2 is taken as 3 (see ref. [6]). In all the numerical computations performed in the present study, it has been assumed that $m_1=m_2=m$. The corresponding permeability expressions are of the form

$$K_1=\frac{m\varepsilon^3}{(1-\varepsilon)^2} \tag{6a}$$

and

$$K_2=\frac{m\varepsilon^3}{(1-\varepsilon)^{0.75}} \tag{6b}$$

where the constant m can be taken to be a characteristic parameter of the alloy system.

Having obtained the permeabilities K_1 and K_2 in the principal directions, it still remains to determine what the principal directions are, at any location in the mushy zone. It can be argued that the primary dendrite direction should be along the local normal to the isotherm passing through the point, since dendrites tend to grow in that direction [12]. Similarly, the transverse direction for the dendrites can be taken parallel to the isotherm. Thus, permeability can be defined as a tensor

$$\underline{\underline{K}}=\begin{bmatrix}K_1 & 0\\ 0 & K_2\end{bmatrix} \tag{7}$$

in the coordinate system of the principal directions. For a global Cartesian system, the permeability can be represented as

$$\underline{\underline{K}}=\begin{bmatrix}K_{xx} & K_{xy}\\ K_{yx} & K_{yy}\end{bmatrix} \tag{8}$$

where the tensorial components K_{xx}, $K_{xy}(=K_{yx})$ and

K_{xy} can be obtained using the rules of tensorial transformation.

It is more convenient to use the non-dimensional 'matrix-resistivity' tensor $\underline{\underline{R}}$ in place of the permeability tensor in the flow equations. Defining

$$\underline{\underline{R}} = m[\underline{\underline{K}}]^{-1} \tag{9}$$

it can easily be verified that $\underline{\underline{R}}$ is dimensionless and depends only upon the local porosity. The components of $\underline{\underline{R}}$ are given by

$$R_{xx} = m\left[\frac{K_1+K_2}{2K_1K_2} - \frac{K_1-K_2}{2K_1K_2}\cos 2\gamma\right] \tag{10a}$$

$$R_{yy} = m\left[\frac{K_1+K_2}{2K_1K_2} + \frac{K_1-K_2}{2K_1K_2}\cos 2\gamma\right] \tag{10b}$$

$$R_{xy} = R_{yx} = -m\frac{K_1-K_2}{2K_1K_2}\sin 2\gamma. \tag{10c}$$

In the above expressions, γ is the angle made by the primary dendrite direction with the x-axis (Fig. 1) and it is given by

$$\tan\gamma = \left(\frac{\partial T}{\partial y}\Big/\frac{\partial T}{\partial x}\right) \tag{11}$$

where $\partial T/\partial x$ and $\partial T/\partial y$ are the local directional derivatives of the temperature field.

With regard to the energy equation, suitable approximations are to be invoked for evaluating the enthalpies h and h_l, and also the porous medium density ρ and the effective thermal conductivity k. It is important to note that ρ and k are volume-averaged properties while enthalpy and specific heat are mass-averaged. Thus, the properties for the mushy zone can be written in terms of the corresponding values of the liquid and solid phases as follows

$$\rho = \varepsilon\rho_l + (1-\varepsilon)\rho_s \tag{12a}$$

$$k = \varepsilon k_l + (1-\varepsilon)k_s \tag{12b}$$

$$c = \frac{\varepsilon\rho_l c_l + (1-\varepsilon)\rho_s c_s}{\rho} \tag{12c}$$

and

$$h = \frac{\varepsilon\rho_l h_l + (1-\varepsilon)\rho_s h_s}{\rho}. \tag{12d}$$

However, the key relationship still needed is the one between the liquid fraction, the local temperature and the local concentration. For dilute systems, the properties such as density and conductivity can be taken as functions of temperature only, since a small quantity of the alloying component is not expected to alter the values significantly. An additional simplification which is highly useful, is the linear dependence of density upon temperature in the mushy-zone. For many alloy systems, the change in density from solid to liquid is not large. For instance, mild steel undergoes roughly 6% increase in density upon solidification. In view of the small change in density, a linearization may be justified. Considering constant densities for solid and liquid phases, the density variation can be represented as shown in Fig. 2(a). Referring to the figure, the lever rule leads to the expression

$$\rho = \rho_s\frac{T-T_l}{T_s-T_l} + \rho_l\frac{T-T_s}{T_l-T_s}. \tag{13}$$

Comparing expressions (12a) and (13), the liquid fraction ε can be written as

$$\varepsilon = \frac{T-T_s}{T_l-T_s}. \tag{14}$$

The enthalpy vs temperature relationship is of the form depicted in Fig. 2(b). The latent heat of solidification is obviously a function of temperature and can be written in a general form as

$$\lambda(T) = h_f + \int_{T_s}^{T} c_l\,dT - \int_{T_s}^{T} c_s\,dT \tag{15}$$

with

$$h_f = \lambda(T_s). \tag{16}$$

The liquid enthalpy h_l is given by

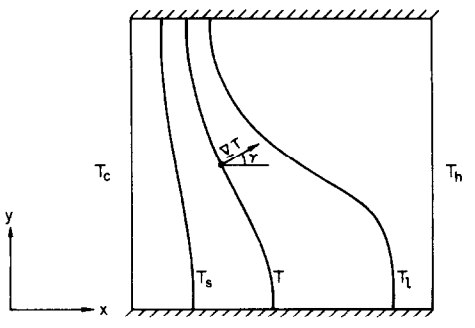

FIG. 1. Approximate direction of growth of primary dendrite at a point in the mushy zone.

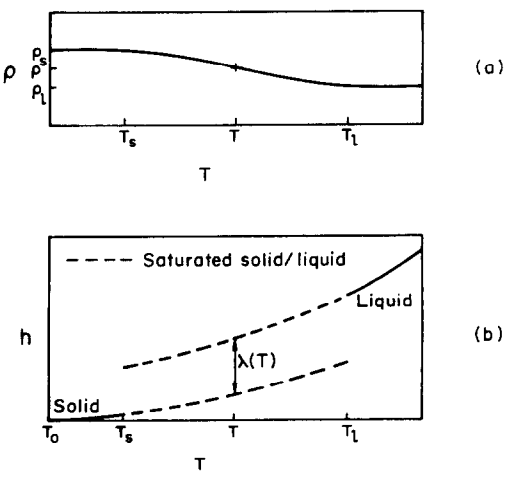

FIG. 2. Variation of density (ρ) and enthalpy (h) with temperature.

$$h_l(T) = \int_{T_0}^{T} c_s \, dT + \lambda(T) \tag{17}$$

where the enthalpy of solid is assumed to be zero at temperature T_0. For the sake of convenience, the value of T_0 can be set equal to zero. Using constant values of specific heats in both the phases, the following relations are obtained

$$\lambda(T) = h_f + (c_l - c_s)(T - T_s) \tag{18}$$

and

$$h_l(T) = c_s T + \lambda(T). \tag{19}$$

The mixture enthalpy at a location in the mushy zone is given by

$$h = \frac{\rho_s(1-\varepsilon)c_s T + \rho_l \varepsilon h_l}{\rho}. \tag{20}$$

Using the above-described functional dependences for properties, the non-dimensional equations can be derived as

$$\frac{\partial \sigma_1}{\partial \tau} + \frac{\partial U}{\partial X} + \frac{\partial V}{\partial Y} = 0 \tag{21}$$

$$\sigma_1 \frac{\partial}{\partial \tau}\left(\frac{U}{\sigma_1}\right) + U\frac{\partial}{\partial X}\left(\frac{U}{\sigma_1}\right) + V\frac{\partial}{\partial Y}\left(\frac{U}{\sigma_1}\right) = -\frac{\partial P}{\partial X} + Pr\left[\frac{\partial}{\partial X}\left\{\sigma_1 \frac{\partial}{\partial X}\left(\frac{U}{\sigma_1}\right)\right\} + \frac{\partial}{\partial Y}\left\{\sigma_1 \frac{\partial}{\partial Y}\left(\frac{U}{\sigma_1}\right)\right\}\right] - M(R_{xx}U + R_{xy}V) \tag{22}$$

$$\sigma_1 \frac{\partial}{\partial \tau}\left(\frac{V}{\sigma_1}\right) + U\frac{\partial}{\partial X}\left(\frac{V}{\sigma_1}\right) + V\frac{\partial}{\partial Y}\left(\frac{V}{\sigma_1}\right) = -\frac{\partial P}{\partial Y} + Pr\left[\frac{\partial}{\partial X}\left\{\sigma_1 \frac{\partial}{\partial X}\left(\frac{V}{\sigma_1}\right)\right\} + \frac{\partial}{\partial Y}\left\{\sigma_1 \frac{\partial}{\partial Y}\left(\frac{V}{\sigma_1}\right)\right\}\right] - M(R_{yx}U + R_{yy}V) + Ra\, Pr\, \theta \tag{23}$$

$$(\sigma_2 + A\sigma_3)\frac{\partial \theta}{\partial \tau} + U\frac{\partial \theta}{\partial X} + V\frac{\partial \theta}{\partial Y} = \frac{\partial}{\partial X}\left(k^*\frac{\partial \theta}{\partial X}\right) + \frac{\partial}{\partial Y}\left(k^*\frac{\partial \theta}{\partial Y}\right) + \sigma_4 \frac{\partial \sigma_1}{\partial \tau} \tag{24}$$

where

$$X = \frac{x}{L}, \quad Y = \frac{y}{L}, \quad U = \frac{uL}{\alpha_0}, \quad V = \frac{vL}{\alpha_0}, \quad \tau = \frac{\alpha_0 t}{L^2}$$

$$P = \frac{pL^2}{\rho_l \alpha_0^2}, \quad \theta = \frac{T - T_{ref}}{T_h - T_c}, \quad M = \frac{\nu_l L^2}{m\alpha_0}, \quad Pr = \frac{\nu_l}{\alpha_0}$$

$$Ra = \frac{gL^3\beta(T_h - T_c)}{\alpha_0 \nu_l}, \quad \alpha_0 = \frac{k_0}{\rho_l c_l}$$

$$k^* = \frac{k}{k_0}, \quad \nu_l = \frac{\mu_l}{\rho_l}, \quad \sigma_1 = \frac{\rho}{\rho_l}, \quad \sigma_2 = \frac{\rho c}{\rho_l c_l}$$

$$\sigma_3 = \frac{\rho_l h_f + (\rho_l - \rho_s)c_s T_s}{\rho_l c_l (T_l - T_s)} + \left\{1 - \frac{\rho_s c_s}{\rho_l c_l}\right\}\varepsilon$$

$$\sigma_4 = \frac{c_s T_s + h_f + c_l(T_l - T_s)\varepsilon}{c_l(T_h - T_c)}$$

$$\varepsilon = \begin{cases} 1 & \text{for} \quad \theta \geqslant \theta_l \\ \dfrac{\theta - \theta_s}{\theta_l - \theta_s} & \text{for} \quad \theta_s \leqslant \theta \leqslant \theta_l \\ 0 & \text{for} \quad \theta \leqslant \theta_s \end{cases}$$

and

$$A = \begin{cases} 1 & \text{when} \quad \theta_s \leqslant \theta \leqslant \theta_l \\ 0 & \text{otherwise} \end{cases}. \tag{25}$$

For the rectangular enclosure (Fig. 3) the following boundary conditions have been applied. Referring to Fig. 3

$$\left.\begin{matrix} U = V = 0 \\ \theta = -1 \end{matrix}\right\} \quad \text{for} \quad X = 0, \quad 0 \leqslant Y \leqslant As \tag{26a}$$

$$\left.\begin{matrix} U = V = 0 \\ \dfrac{\partial \theta}{\partial Y} = 0 \end{matrix}\right\} \quad \text{for} \quad Y = 0, \quad 0 \leqslant X \leqslant 1 \tag{26b}$$

$$\left.\begin{matrix} U = V = 0 \\ \theta = 0 \end{matrix}\right\} \quad \text{for} \quad X = 1, \quad 0 \leqslant Y \leqslant As \tag{26c}$$

$$\left.\begin{matrix} U = V = 0 \\ \dfrac{\partial \theta}{\partial Y} = 0 \end{matrix}\right\} \quad \text{for} \quad Y = As, \quad 0 \leqslant X \leqslant 1. \tag{26d}$$

The initial conditions are

$$U = V = \theta = 0 \quad \text{at} \quad \tau = 0. \tag{26e}$$

The generalized formulation presented above

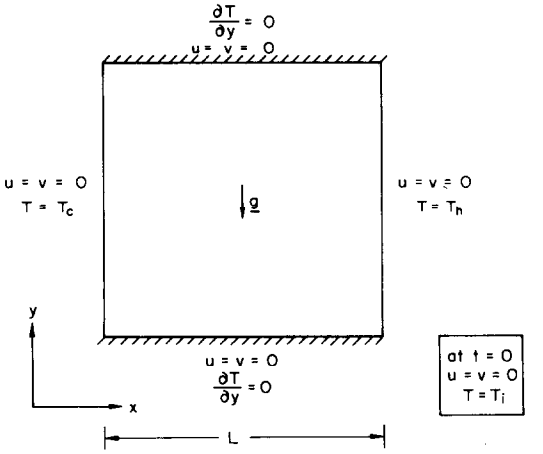

FIG. 3. Problem geometry with boundary and initial conditions.

involves constant dimensionless parameters such as Ra, Pr, M, θ_s, θ_l, k_s/k_0 and k_l/k_0 as well as the dimensionless variable coefficients σ_1, σ_2, σ_3 and σ_4 whose values change across the mushy zone. For the parametric study, the densities and the specific heats have been taken to be equal for both the phases and this leads to the simplification

$$\sigma_1 = 1, \quad \sigma_2 = 1 \quad \text{and} \quad \sigma_3 = Ste = \frac{h_f}{c_1(T_l - T_s)}.$$

A summary of all the property/parameter values used in the numerical calculations is provided in Table 1.

SOLUTION PROCEDURE

The governing equations (21)–(25) have been solved numerically subject to the boundary and initial conditions (26a)–(26e), along with permeability calculations via equations (10) and (11). An implicit time marching procedure coupled with the finite element method (FEM) has been employed. Although a simple rectangular geometry has been studied herein, a general 2-D/axisymmetric code has been developed which can easily be applied to any arbitrary geometry. The choice of FEM has specific advantages for the modelling of the alloy solidification problem. In view of the powerful interpolation and numerical integration schemes employed in FEM, property variations can be accounted for even within a single element.

Eight-noded serendipity type elements have been used to discretize the solution domain. Temperature and velocity variations have been interpolated with quadratic functions while pressure has been interpolated linearly within each element. The elemental interpolation schemes can be expressed in terms of the nodal variable values as

$$U = \sum_{j=1}^{8} N_j U_j, \quad V = \sum_{j=1}^{8} N_j V_j$$
$$\theta = \sum_{j=1}^{8} N_j \theta_j, \quad P = \sum_{j=1}^{4} M_j P_j \qquad (27)$$

where N_j, M_j are the quadratic and linear shape functions respectively. The lower-degree interpolation for pressure is necessary in order to avoid spurious oscillations in the pressure field [13].

Table 1. Test problem data

As	1.0
k_s/k_0	1.0, 1.5
k_l/k_0	1.0, 0.5
M	10^6
Pr	10^3
Ra	10^3, 10^4, 10^5
Ste	8.3
U_{init}	0.0
V_{init}	0.0
θ_{init}	0.0
θ_c	−1.0
θ_h	0.0
θ_s	−0.6, −0.8
θ_l	−0.4, −0.2

Galerkin's weighted residual approach has been used to derive the matrix equations for solving the nodal values of velocity, temperature and pressure. The residue equations are given by

$$\iint_\Omega M_i(\nabla \cdot \mathbf{V})\,dX\,dY = [0] \qquad (28)$$

$$\iint_\Omega N_i\left(\frac{\partial \mathbf{V}}{\partial \tau} + \mathbf{V}\cdot\nabla\mathbf{V} + \nabla P - Pr\,\nabla^2\mathbf{V} + M\underline{\underline{R}}\cdot\mathbf{V} - Ra\,Pr\,\theta\hat{j}\right)dX\,dY = [0] \qquad (29)$$

$$\iint_\Omega N_i\left((1 + A\,Ste)\frac{\partial \theta}{\partial \tau} + \mathbf{V}\cdot\nabla\theta - \nabla\cdot(k^*\nabla\theta)\right)dX\,dY = [0]. \qquad (30)$$

Applying integration by parts to the viscous and conduction terms of equations (29) and (30), and substituting the interpolation expressions of equation (27), the final matrix equations are obtained in the form

$$\sum_{e=1}^{E}\begin{bmatrix} C_{11} & C_{12} & C_{13} & C_{14} \\ C_{21} & C_{22} & C_{23} & C_{24} \\ C_{31} & C_{32} & C_{33} & C_{34} \\ C_{41} & C_{42} & C_{43} & C_{44} \end{bmatrix}_{ij}\begin{Bmatrix} U \\ P \\ V \\ \theta \end{Bmatrix}_j = \sum_{e=1}^{E}\begin{bmatrix} f_1 & 0 & 0 & 0 \\ 0 & f_2 & 0 & 0 \\ 0 & 0 & f_3 & 0 \\ 0 & 0 & 0 & f_4 \end{bmatrix}_{ij}\begin{Bmatrix} U^0 \\ P^0 \\ V^0 \\ \theta^0 \end{Bmatrix}_j \qquad (31)$$

where the coefficient matrices on the left-hand and right-hand sides of equation (31) represent sub-matrices corresponding to the different nodes of the element. These sub-matrices, when assembled for all values of i and j, form the elemental contributions to the global matrix equation. The sub-matrix entries are themselves given by

$$C_{11} = \iint_{A^e}\left[\frac{N_i N_j}{\Delta\tau} + N_i\tilde{U}\frac{\partial N_j}{\partial X} + N_i\tilde{V}\frac{\partial N_j}{\partial Y} + Pr\left(\frac{\partial N_i}{\partial X}\frac{\partial N_j}{\partial X} + \frac{\partial N_i}{\partial Y}\frac{\partial N_j}{\partial Y}\right) + MR_{XX}N_iN_j\right]dX\,dY$$

$$C_{12} = \iint_{A^e} N_i\frac{\partial M_j}{\partial X}\,dX\,dY$$

$$C_{13} = \iint_{A^e} MR_{XY}N_iN_j\,dX\,dY$$

$$C_{14} = 0$$

$$C_{21} = \iint_{A^e} M_i \frac{\partial N_j}{\partial X} \mathrm{d}X\,\mathrm{d}Y$$

$$C_{22} = C_{24} = 0$$

$$C_{23} = \iint_{A^e} M_i \frac{\partial N_j}{\partial Y} \mathrm{d}X\,\mathrm{d}Y$$

$$C_{31} = C_{13}$$

$$C_{32} = \iint_{A^e} N_i \frac{\partial M_j}{\partial Y} \mathrm{d}X\,\mathrm{d}Y$$

$$C_{33} = \iint_{A^e} \left[\frac{N_i N_j}{\Delta\tau} + N_i \tilde{U} \frac{\partial N_j}{\partial X} + N_i \tilde{V} \frac{\partial N_j}{\partial Y} + Pr \left(\frac{\partial N_i}{\partial X} \frac{\partial N_j}{\partial X} + \frac{\partial N_i}{\partial Y} \frac{\partial N_j}{\partial Y} \right) + MR_{YY} N_i N_j \right] \mathrm{d}X\,\mathrm{d}Y$$

$$C_{34} = \iint_{A^e} -Ra\,Pr\,N_i N_j\,\mathrm{d}X\,\mathrm{d}Y$$

$$C_{41} = C_{42} = C_{43} = 0$$

$$C_{44} = \iint_{A^e} \left[(1 + A\,Ste) \frac{N_i N_j}{\Delta\tau} + N_i \tilde{U} \frac{\partial N_j}{\partial X} + N_i \tilde{V} \frac{\partial N_j}{\partial Y} + k^* \left(\frac{\partial N_i}{\partial X} \frac{\partial N_j}{\partial X} + \frac{\partial N_i}{\partial Y} \frac{\partial N_j}{\partial Y} \right) \right] \mathrm{d}X\,\mathrm{d}Y$$

$$f_1 = \iint_{A^e} \frac{N_i N_j}{\Delta\tau} \mathrm{d}X\,\mathrm{d}Y$$

$$f_2 = 0$$

$$f_3 = f_1$$

$$f_4 = \iint_{A^e} (1 + A\,Ste) \frac{N_i N_j}{\Delta\tau} \mathrm{d}X\,\mathrm{d}Y. \tag{32}$$

The shape function index i takes values 1–8 for the momentum/energy equations and 1–4 for the continuity equation. The index j assumes values 1–8 when it is associated with the variables U, V and θ, and 1–4 for pressure. The elemental matrices are assembled for all the elements of the domain and the resulting matrix system is solved using the frontal technique [14]. In view of the strong non-linearities exhibited by the governing equations, a Picard-type iterative scheme with under-relaxation has been employed, to march from one time level to another.

A mesh of 10×10 elements has been used to simulate the results. The correctness of the numerical solutions has been checked by a bench-mark comparison with the known Neumann solution for a pure metal system with constant properties and the details are reported elsewhere [9]. The CPU time taken for a typical run was of the order of 3 min per time step on HP-9000 series computer network.

RESULTS AND DISCUSSION

Results have been obtained for the range of parameters covering $Ra = 10^3$, 10^4, 10^5; conductivity ratios $k_l/k_0 = 1.0, 0.5$; $k_s/k_0 = 1.0, 1.5$; liquidus temperature $\theta_l = -0.4$, -0.2 and solidus temperature $\theta_s = -0.6$, -0.8. Both anisotropic and isotropic mushy zone permeabilities have been considered and results have been presented in the form of comparisons between the two situations. A constant Prandtl number has been considered since even a large variation of this parameter does not have much effect upon the heat transfer or fluid flow [9]. Also, the parameter Ste has not been varied as it influences only the transient evolution of solutions in a straight forward manner.

The progress of the solidification fronts (liquidus and solidus) with time is shown in Figs. 4(a)–(d). It is observed that for small times, the curvature of the liquidus front is small implying the predominance of conduction heat transfer. For later times, convection in the mushy zone as well as the fully-liquid region becomes vigorous and therefore the liquidus front assumes a curved shape; however, the solidus front still remains flat in view of the small velocities in its neighbourhood. For non-dimensional time of the order of unity, the progress of the fronts is arrested and a steady state configuration is reached. This is an expected feature for a rectangular enclosure with two isothermal and two adiabatic walls. It is also evident that the extent of mushy zone increases with time, implying a faster rate of movement for the liquidus front due to convective heat transfer.

A comparison between the isotropic and anisotropic situations indicates that the phase fronts are less distorted when anisotropic permeability is considered. However, the mean rates of movement of these fronts are not very much affected. Thus, the overall impact of anisotropy of the mushy zone permeability appears to be the alteration of the shape of the liquidus (and, to a small extent, the solidus) phase front.

In Figs. 5 and 6 the effects of the mushy zone size upon the resulting isothermal patterns are compared for isotropic and anisotropic situations. Figure 5 corresponds to dimensionless liquidus and solidus temperatures of -0.4 and -0.6 respectively. Figure 6, on the other hand, corresponds to $\theta_l = -0.2$ and $\theta_s = -0.8$. It is clear from the two figures that anisotropic effects are significant only when the mushy zone is larger. Indeed, at lower Rayleigh numbers, there is hardly any difference between the isotropic and anisotropic cases for smaller mushy range. It is worthwhile mentioning here the physical significance of choosing different values for θ_s and θ_l. Although the liquidus and solidus temperatures are constants for a particular alloy system of given concentration, the

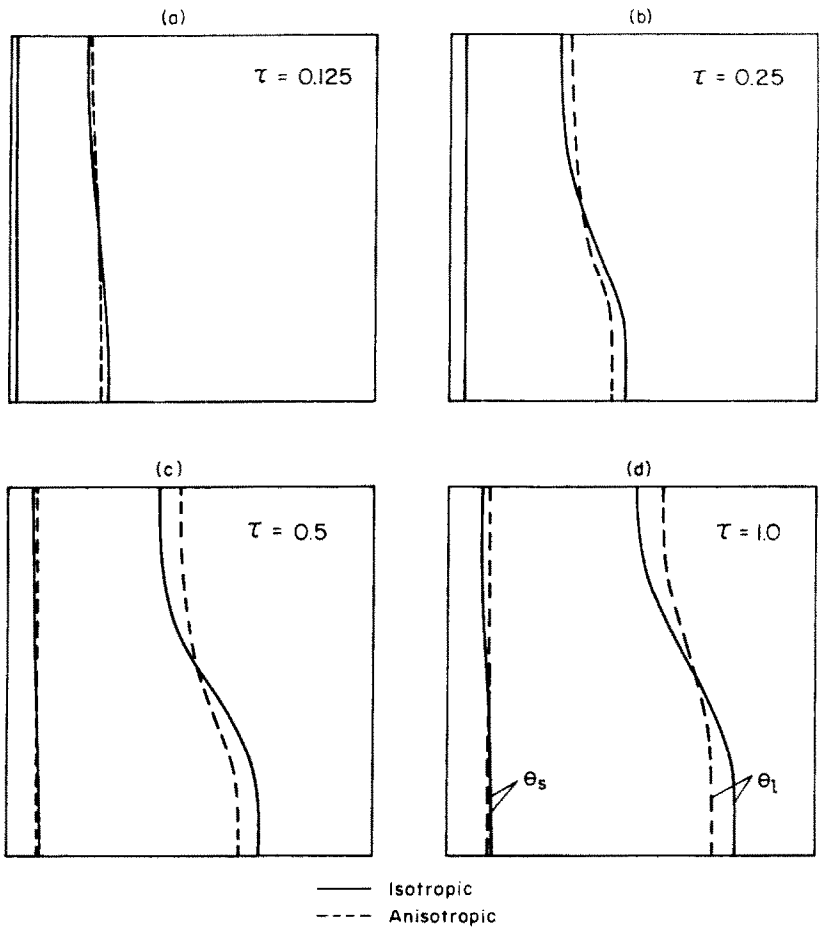

FIG. 4. Progress of liquidus and solidus with time for isotropic and anisotropic cases.

non-dimensional values θ_l and θ_s could be different depending upon the actual temperatures of the isothermal walls. Thus, for the same alloy system, the larger range of mushy zone implies a smaller difference between the wall temperatures. Further, the actual sizes of the cavities may be different between Figs. 5 and 6, in order to have the same Rayleigh numbers at different values of $T_h - T_c$. Thus, a variety of parameter combinations could lead to a larger or a smaller mushy zone. In the present study, in order to highlight the effects of property variation, a larger mushy zone has been considered with $\theta_l = -0.2$ and $\theta_s = -0.8$.

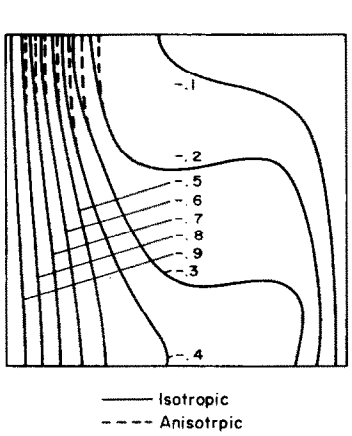

FIG. 5. Effect of anisotropy on isothermal patterns for smaller mushy zone.

The flow fields for the isotropic and anisotropic situations are depicted in Figs. 6(b), (c) respectively for $Ra = 10^5$. The velocities are larger in magnitude for the isotropic situation, particularly in the mushy zone. This explains the reason for the larger curvature observed in the shapes of the phase fronts and other isotherms for the isotropic situation. In Figs. 7(a), (b) the directional permeabilities (K_1 and K_2) and the porosity have been plotted in the mushy zone. The permeability values are extremely large (approaching infinity) near the liquidus and decrease sharply towards the solidus, where they are zero. Along the isotherms, the permeability values are smaller by an order of magnitude as compared to the direction nor-

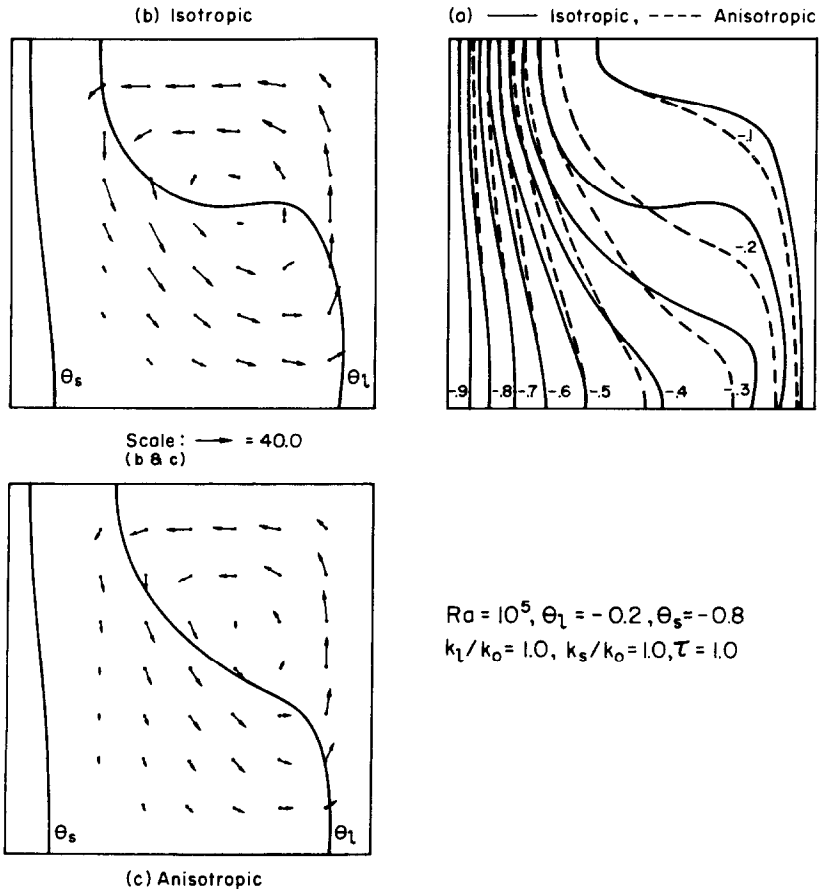

FIG. 6. Effect of anisotropy on temperature and velocity fields at $Ra = 10^5$.

mal to the isotherms. The fact that the permeability is much less in the approximate direction of flow within the mushy zone results in smaller flow velocities for the anisotropic case. With respect to porosity variation, it may be said that the gradient of porosity is large at the top portion of the mushy zone as compared to the bottom region. Therefore, flow effects are significant only in the middle and bottom portions of

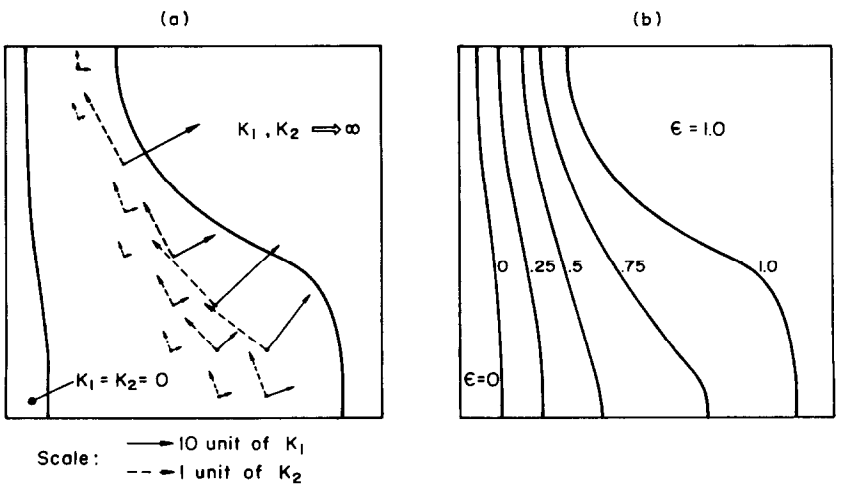

$Ra = 10^5, \theta_l = -0.2, \theta_s = -0.8, k_l/k_o = 1.0, k_s/k_o = 1.0, \tau = 1.0$

FIG. 7. Directional permeabilities (K_1, K_2) and isoporosity lines (ε = constant) for anisotropic situation.

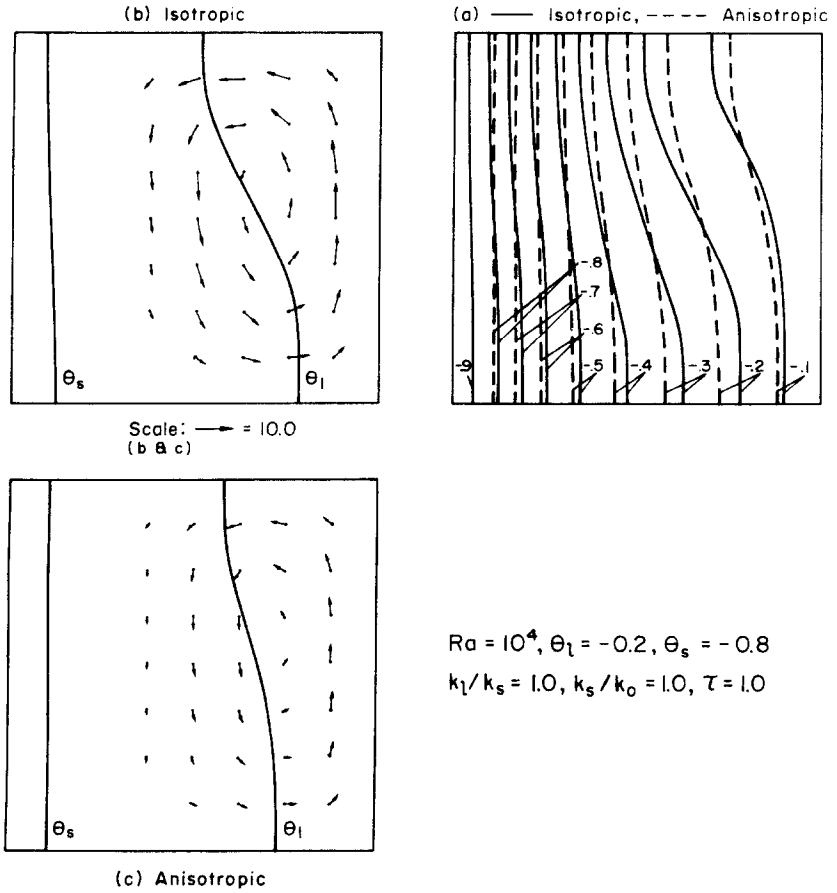

FIG. 8. Effect of anisotropy on temperature and velocity fields at $Ra = 10^4$.

the mushy zone adjacent to the liquid and the curvature of the isotherms also occurs in these portions only.

The effects of Rayleigh number upon the flow fields and the isotherms can be seen from Figs. 6, 8 and 9. The magnitude of the velocity vectors considerably increases with Rayleigh number, indicating that the convective flow becomes more and more vigorous. It is also observed that the velocities are smaller for the anisotropic case for all Rayleigh numbers. A careful examination reveals that the fluid flow tends to adjust itself so as to minimize the residence time within the mushy zone. For instance, at $Ra = 10^3$ and 10^4, the mushy zone is nearly of rectangular geometry. The stream lines which pass through the mushy zone and the liquid region are approximately elliptical for these cases. At $Ra = 10^5$, however, the shape of the mushy zone on the liquidus side is considerably inclined to the vertical, around the central portion. The flow lines adjacent to this boundary also assume a nearly triangular shape with a tendency for least residence in the mushy zone. The isotherms in the mushy and liquid regions become increasingly more distorted at higher Rayleigh numbers due to convective effects. The difference in isotherm shapes between the isotropic and anisotropic situations also increases with Rayleigh number.

The effect of thermal conductivity ratios upon the isothermal pattern is shown in Figs. 10(a), (b). When solid conductivity is larger than that of the liquid, the rate of solidification is faster at all Rayleigh numbers. The shapes of the isotherms are essentially the same with only shift in their positions for different conductivity ratios.

The Nusselt number variation along the hot isothermal wall is shown in Figs. 11(a), (b). For high Rayleigh numbers, the Nusselt number is high in the bottom region, with a tendency for the formation of a thermal boundary layer. As expected, Nusselt number is smaller in magnitude for the anisotropic case due to smaller flow velocities. As Rayleigh number is reduced, the Nusselt number variation along the surface becomes negligible, approaching the conduction limit. In fact, there is hardly any difference between the isotropic and anisotropic situations for low Rayleigh number. For large Rayleigh number, the wall Nusselt number at the top portion decreases below the conduction limit; this is due to reduction in heat transfer caused by the prior heating of the fluid in the bottom portion. The rate of heat

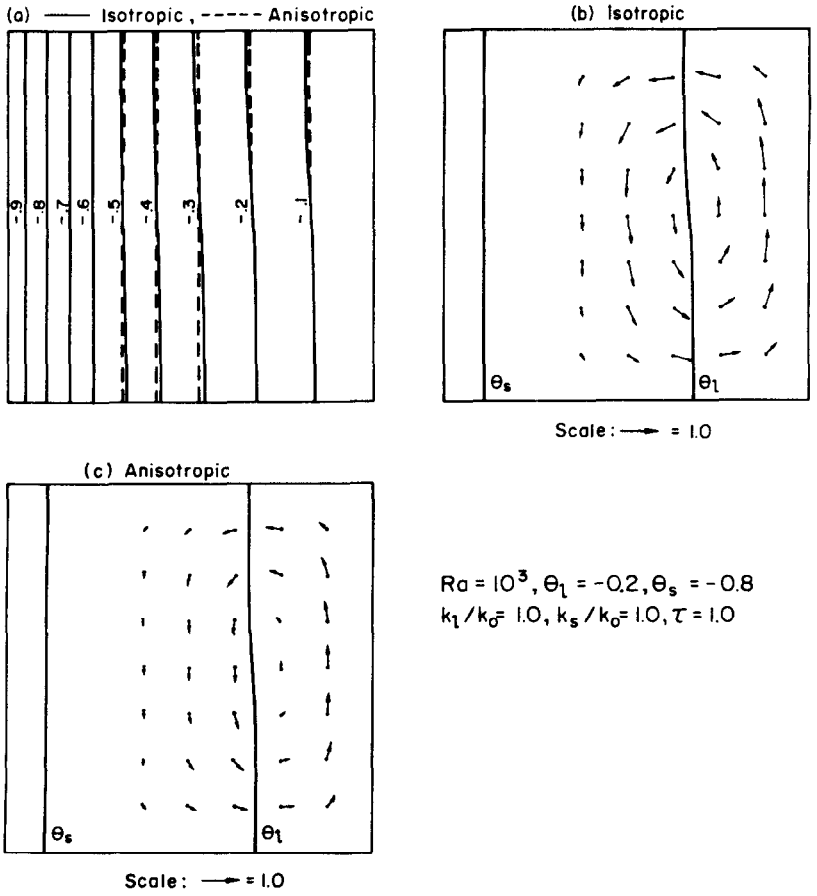

FIG. 9. Effect of anisotropy on temperature and velocity fields at $Ra = 10^3$.

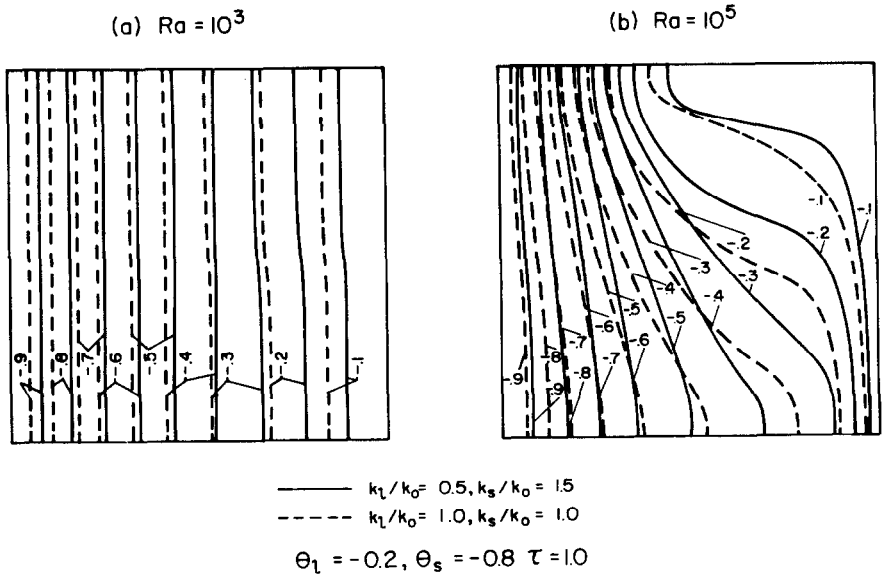

FIG. 10. Effect of solid and liquid thermal conductivity ratios upon isothermal patterns at (a) $Ra = 10^3$ and (b) $Ra = 10^5$, for anisotropic case.

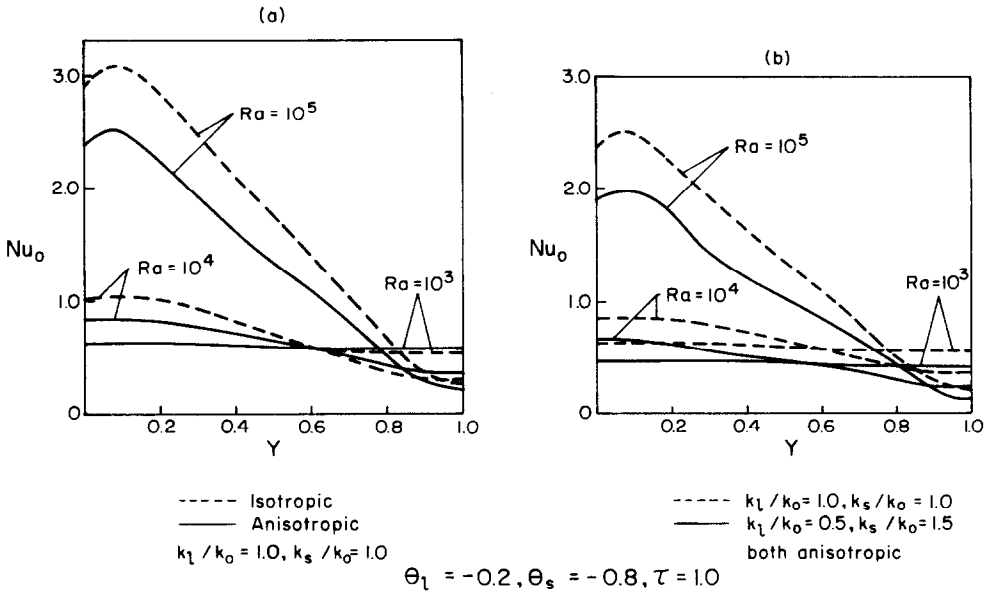

FIG. 11. Nusselt number variation along the hot wall at different Rayleigh numbers and thermal conductivity ratios, for isotropic and anisotropic situations.

transfer on the liquid side decreases for smaller k_l as expected.

CONCLUSIONS

A variable property analysis has been developed for the dendritic solidification of a dilute alloy, using the porous medium approach. Giving due consideration to the dendritic structure of the phase-change region, an anisotropic permeability variation has been incorporated. A detailed parametric study of the two-dimensional solidification within a rectangular enclosure has been performed. The influence of anisotropy is seen to be significant for large mushy zones as well as at high Rayleigh numbers.

REFERENCES

1. D. K. Gartling, Finite element analysis of convective heat transfer problems with change of phase. In *Computer Methods in Fluids* (Edited by K. Morgan, C. Taylor and C. A. Brebbia), pp. 257–284. Pentech, London (1980).
2. K. Morgan, A numerical analysis of freezing and melting with convection, *Comp. Meth. Appl. Mech. Engng* **28,** 275–284 (1981).
3. R. Mehrabian, Interdendritic fluid flow and macrosegregation; influence of gravity, *Metall. Trans.* **1,** 1209–1220 (1970).
4. W. D. Bennon and F. P. Incropera, Numerical analysis of binary solid–liquid phase change using a continuum model, *Numer. Heat Transfer* **13,** 277–296 (1988).
5. V. R. Voller, A. D. Brent and C. Prakash, The modelling of heat, mass and solute transport in solidification systems, *Int. J. Heat Mass Transfer* **32,** 1719–1731 (1989).
6. D. R. Poirier, Permeability for flow of interdendritic liquid in columnar-dendritic alloys, *Metall. Trans.* **18B,** 245–255 (1987).
7. H. C. Brinkman, A calculation of the viscous force exerted by a flowing fluid on a dense swarm of particles, *Appl. Scient. Res.* **A1,** 27–34 (1947).
8. K. Yamamoto and N. Iwamura, Flow with convective acceleration through a porous medium, *J. Engng Math.* **10** (1976).
9. S. K. Sinha and T. Sundararajan, Analysis of alloy solidification inside arbitrary-shaped two-dimensional enclosures (to be published).
10. W. D. Bennon and F. P. Incropera, A continuum model for momentum, heat and species transport in binary solid–liquid phase change systems—1. Model formulation, *Int. J. Heat Mass Transfer* **30,** 2161–2170 (1987).
11. V. R. Voller and C. Prakash, A fixed grid numerical modelling methodology for convection diffusion mushy region phase-change problems, *Int. J. Heat Mass Transfer* **30,** 1709–1719 (1987).
12. M. C. Flemings, *Solidification Processing*. McGraw-Hill, New York (1974).
13. C. P. Jackson and K. A. Cliffe, Mixed interpolation in primitive variable finite element formulations for incompressible flow, *Int. J. Numer. Meth. Engng* **17** (1980).
14. C. Taylor and T. G. Hughes, *Finite Element Programming of the Navier–Stokes Equations*. Pineridge Press, Swansea (1981).

ANALYSE DE PROPRIETES VARIABLES DANS LA SOLIDIFICATION D'UN ALLIAGE UTILISANT L'APPROCHE DE MILIEU POREUX ANISOTROPE

Résumé—On présente un modèle théorique du transfert de chaleur et de l'écoulement pendant la solidification d'un alliage. On a tenu compte en détail des variations des propriétés dans la région de changement de phase dendritique. On adopte une approche de milieu poreux avec variation de la perméabilité qui est anisotrope. Les effets de l'anisotropie sont observés être significatifs si l'étendue de la zone boueuse est grande ou si le nombre de Rayleigh est élevé.

UNTERSUCHUNG DER ERSTARRUNG VON LEGIERUNGEN MIT VARIABLEN STOFFEIGENSCHAFTEN UNTER VERWENDUNG EINER NÄHERUNG FÜR ANISOTROPE PORÖSE MEDIEN

Zusammenfassung—Es wird ein theoretisches Modell für Wärmeübergang und Strömung bei der Erstarrung von Legierungen vorgestellt. Die Veränderung der Stoffeigenschaften in dem kritischen Phasenänderungsgebiet wird detailliert berücksichtigt. Es wird eine verallgemeinerte Näherung für poröse Medien angewandt, jedoch mit einer anisotropen Permeabilität. Die Einflüsse der Anisotropie erweisen sich als wesentlich, wenn die Erstarrungszone sehr ausgedehnt ist oder wenn die Rayleigh-Zahl groß ist.

АНАЛИЗ ПЕРЕМЕННЫХ СВОЙСТВ ПРИ ЗАТВЕРДЕВАНИИ СПЛАВА С ИСПОЛЬЗОВАНИЕМ МОДЕЛИ АНИЗОТРОПНЫХ ПОРИСТЫХ СРЕД

Аннотация—Представлена теоретическая теплопереноса и течения жидкости в процессе затвердевания сплава. Подробно исследуются изменения свойств на дендритном участке фазового перехода. Используется обобщенная модель пористых сред с анизотропной проницаемостью. Обнаружено, что влияние анизотропности является существенным при большой протяженности двухфазной зоны или при числе Рэлея.